optica

Topological transformation of speckles: supplementary materials

JÉRÔME GATEAU[1]**, FERDINAND CLAUDE**[2]**, GILLES TESSIER**[2,3]**, AND MARC GUILLON**[2,4,*]

[1]*Sorbonne Université, CNRS, INSERM, Laboratoire d'Imagerie Biomédicale, LIB, 15 rue de l'école de Médecine, F-75006, Paris, France*
[2]*Neurophotonics Laboratory, CNRS UMR 8250, Paris Descartes University, Sorbonne Paris Cité, Paris, France*
[3]*Sorbonne Université, Institut de la Vision, INSERM UMR S968, CNRS UMR 7210, 17 rue Moreau, 75012, Paris, France*
[4]*Saint-Pères Paris Institute for Neurosciences (SPPIN), CNRS UMR 8003, Paris Descartes University, Sorbonne Paris Cité, Paris, France*
[*]*Corresponding author: marc.guillon@parisdescartes.fr*

This document provides supplementary information to "Topological transformation of speckles," https://doi.org/10.1364/OPTICA.6.000914. The first section provides expended descriptions of the methods used to acquire and process the experimental data: details are given on the phase mask displayed on the spatial light modulator, the numerical treatment of the recorded speckle patterns is presented, and the algorithms for the detection of critical points are given. The second section contains numerical confirmations of the experimental results, as well as an extension (in numerical simulation) of the range of tested binary amplitude apertures: the Weighted Median Normalized Distances are shown for star-like amplitude masks with dihedral symmetries of orders higher than 4, for star-like amplitude masks with larger angular slits, and for polygonal apertures.

1. EXPERIMENTAL DATA ACQUISITION AND PROCESSING

A. Phase mask on the SLM

The laser source was a laser diode emitting at $\lambda = 635$ mm. The laser beam was spatially filtered with a pinhole, expanded and collimated to cover the surface of the Spatial Light Modulator (SLM). The phase at the SLM was computed according to the scheme shown in Fig. S1.

The scattering phase pattern at the SLM (or diffuser in Fig. S1) was engineered in order to both generate a fully developed speckle pattern at the camera plane and to minimize energy losses by controling the scattering angle. To achieve so, a complex matrix of dimension 396×396 pixels (half of the long-axis of the SLM) was generated numerically, with uniform amplitude and random phases evenly distributed between 0 and 2π. This random matrix was then multiplied by a disk-shaped amplitude mask of radius 60 SLM pixels (SLM pixel size : $px_{SLM}^2 = 20 \times 20$ μm^2) and Fourier transformed numerically to generate the random phase mask at the SLM plane. Provided

the optical design of the setup and the focal distance of the lens $f = 750$ mm, this mask corresponds to a disk of diameter $\frac{60}{400} \times \frac{2.\lambda.f}{px_{SLM}} \simeq 8.8$ mm, slightly larger than the camera diagonal (7.62 mm), so ensuring uniform illumination of the camera chip (on average) and minimization of energy losses.

The BA amplitude mask were applied to the phase mask by setting the SLM phase to zero where the amplitude of the BA mask equals zero, and by adding a blazed grating where the amplitude of the BA mask equals one. The radius of the BA masks was chosen to have a speckle grain size of 15 camera pixels (camera pixel size: 4.65×4.65 μm^2). The blazed grating had a period of 4.34 SLM pixels (SLM pixel size : 20×20 μm^2), which yields a deflection angle of 7.31 mrad. With the focal distance of the lens $f = 750$ mm, this deflection angle provides a 5 mm shift of the zero order as compared to the speckle pattern. Because of the camera field of view (4.76 mm $\times$ 5.95 mm), the undiffracted zero-order was centered at a distance 2.5 mm away from the camera sensor and could then efficiently be blocked with no spurious light observed on the camera.
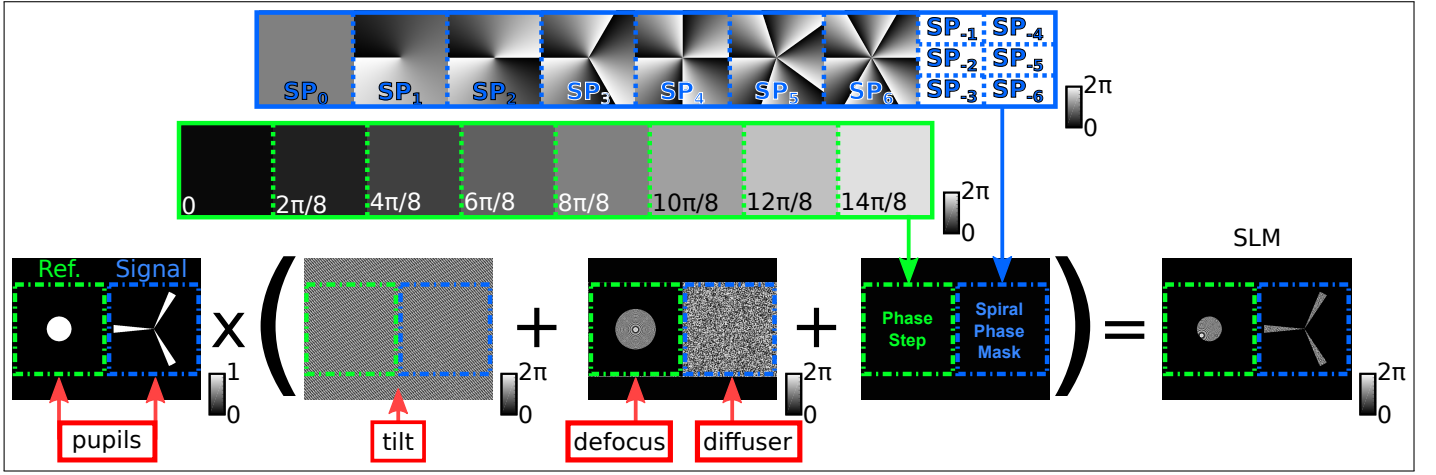
Fig. S1. Computation of the phase displayed at the SLM. The SLM is virtually split into two parts of surfaces 396×396 pixels, each bearing pupils of different shapes, one for the reference beam (green), the other for the signal beam (blue). A tilt is applied to both beams in order to shift the speckle pattern of interest away from the unmodulated light. A defocus is added to the reference beam to cover the caerma surface, while the signal beams receives a random phase mask (or diffuser). Finally, the phase step and spiral wavefronts are added.

For the reference beam, the same blazed grating was applied to a disk-shaped aperture separated from the scattering aperture. The radius of the disk was chosen so that the signal beam (scattered wavefield) and the reference beam have similar amplitudes at the camera plane. A defocus (Fresnel lens) was applied to the reference beam to cover the camera surface.

B. Numerical treatment of experimental data

The complex wavefield $A_n e^{i\Phi_n}$ at the camera plane was measured with the following procedure. The phase Φ_n was obtained thanks to the intensity modulation induced by the phase-stepping interferometric measurements [1, 2]. The phase-stepping was performed by acquiring eight successive images with relative phase-shifts between the signal and reference waves: $k \times 2\pi/N$, with $N = 8$ and $k \in [\![0;7]\!]$. The phase of the speckle pattern was obtained from phase-stepped intensity measurements:

$$
\begin{aligned}
I_{n,k} &= \left| E_R e^{\frac{2ik\pi}{N}} + A_n e^{i\Phi_n} \right|^2 \tag{S1} \\
&= |E_R|^2 + |A_n|^2 + E_R A_n e^{-i\Phi_n} e^{\frac{2ik\pi}{N}} + E_R^* A_n e^{i\Phi_n} e^{-\frac{2ik\pi}{N}}
\end{aligned}
$$

The phase can then be trivially retrieved by computing the argument of the following sum:

$$
\sum_{k=0}^{N-1} I_{n,k} \times e^{\frac{2ik\pi}{N}} = E_R^* A_n e^{i\Phi_n} \tag{S2}
$$

In our case, the reference beam did not exhibit a flat phase but a combination of a parabolic curvature as well as a relative phase tilt with respect to the speckled beam. Both of these profiles were numerically removed from the computed phase Φ_n. The magnitude A_n was not computed using this result to avoid amplitude uncertainties about the reference beam. Instead, A_n was obtained from the signal speckle intensity I_n without any reference beam: $A_n = \sqrt{I_n}$.

For all the apertures and all the speckle patterns, the Full Width Half Maximum (FWHM) of the point spread function (i.e. the speckle grain size) corresponded to 15 camera pixels, leading a fine spatial sampling of the speckle field. We set the length unit

to 15 pixels and the corresponding spatial sampling frequency to 15 pixel^{-1}. For noise removal, the complex amplitude field was filtered in the Fourier domain by zeroing the values corresponding to spatial frequencies outside of the disk $\sqrt{f_x^2 + f_y^2} \leqslant 0.5$ pixel^{-1}. Because of the spatial filtering by optical system, the frequencies outside of this disk contain only optical and electronic noise. We verified that the strongest spectral values of the complex field were within the disk. After this filtering process, experimental noise was not found to interfere with the detection of the critical points.

C. Detection of the critical points

The detection of critical points in the experimental speckle pattern is illustrated in Fig. S2. The pixel-precise locations of the critical points were determined in the spatial domain using the topology of each pixel neighborhood. For the intensity maxima M, the intensity saddles S^I and the phase saddles S^p, the eight neighbors of each pixel were used. We used the Matlab function developed by Tristan Ursell and made available in May 2013 (image extrema finder, https://fr.mathworks.com/matlabcentral/fileexchange/41955-find-image-extrema). For the vortices V^+ and V^-, we used the fact that the summed phase shifts on a closed loop around a vortex is greater than 2π. As a dicretised closed loop, we computed this sum over four neighbouring pixels, the phase differences between the adjacent corners of the square being computed and wrapped in the range $]-\pi, \pi]$. The summed phase shift was computed by adding the four phase differences, leading to a summed phase shift of $\pm 2\pi$ around a vortex of charge ± 1 and a summed phase shift close to zero elsewhere [3].

2. NUMERICAL SIMULATIONS OF SCALAR RANDOM WAVEFIELDS

Numerical simulations of scalar random wavefields were performed to confirm our experimental results with larger statistics on critical points, independent random phase media and an independent method (section 2B). Indeed, larger speckle patterns can be generated numerically directly from randomly distributed
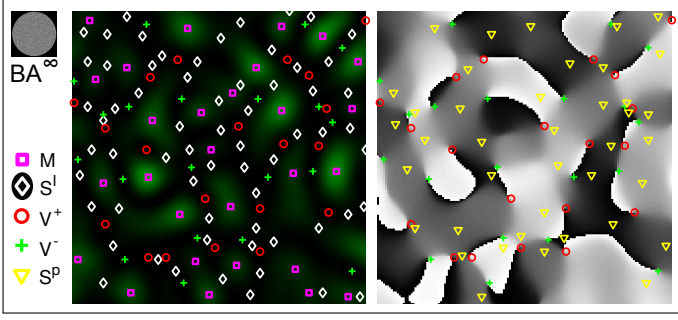
Fig. S2. Detected critical points superimposed to the filtered experimental intensity (left) and phase (right) patterns obtained with the aperture BA^∞. The displayed pattern correspond to an area of 150×150 pixels on the camera. Phase vortices (V^+ and V^-) are also zeros of the intensity pattern. Notations for the critical points are identical to those introduced in the core of the main article.

phase. Additionally, we extended our investigations to apertures with point group symmetries of orders higher than 4 (section 2C), as well as to apertures with larger angular slits (section 2D) and to polygon apertures (section 2E).

A. Methods for the numerical simulation

The far-field of uniformly-illuminated apertures comprised of random phases (standard uniform distribution between 0 and 2π,) with spiral phase (SP) masks of order $n \in [\![-6; 6]\!]$, was computed to simulate the complex wavefield $A_n e^{i\Phi_n}$. The speckle patterns were obtained by computing the two-dimensional Fourier transform of the apertures addressed with random phases. As in the experimental procedure, an uncorrelated speckle pattern was also computed for each aperture. For all the apertures, the speckle grain size (FWHM) was set to $\lambda/(2.NA) = 19$ pixels where λ is the optical wavelength and NA is the numerical aperture, and a square grid of 17 mega pixels was computed. The pixel-precise location of the critical points were determined in the spatial domain using the topology of each pixel neighborhood, as for the experimental speckle patterns.

These parameters lead to a count of critical points for the aperture BA^∞ of $\sim 10^4$ vortices of each sign. The average number-densities of the critical points for the apertures BA^∞, BA^3 and BA^4 are presented in Table S1. The slight differences in number-densities between experimental and simulation measurements can be attributed to the higher number of critical points in the simulation, which leads to better precision in the estimation of the critical point densities.

Table S1. Measured average number density of critical points from numerical simulations (length unit: $\lambda/(2.NA)$). The average number of V^- is 9551.43 for the circular aperture (BA^∞).

BA mask	V^-(or V^+)	M	S^p	S^I
BA^∞	0.20	0.32	0.39	0.67
BA^3	0.21	0.38	0.39	0.75
BA^4	0.20	0.34	0.43	0.70

B. Validation of the experimental results

To support our experimental measurements, numerical simulations were performed for the apertures BA^∞, BA^3 and BA^4. The resulting Weighted Median Normalized Distances (WMND) are presented in Fig. S3. Despite the difference in the method to generate the speckle field, the size of the speckle grains, and the number of critical points involved in the statistical estimation of the WMNDs, our experimental results are remarkably consistent with numerical ones. Our experimental results are then validated in two regards. First, the results are robust to modifications in (i) the method to generate the speckle patterns, (ii) the scattering medium and (iii) the spatial sampling. Second, our experimental estimation of the WMND are statistically relevant since a higher average number of critical points did not lead to significantly different WMND.
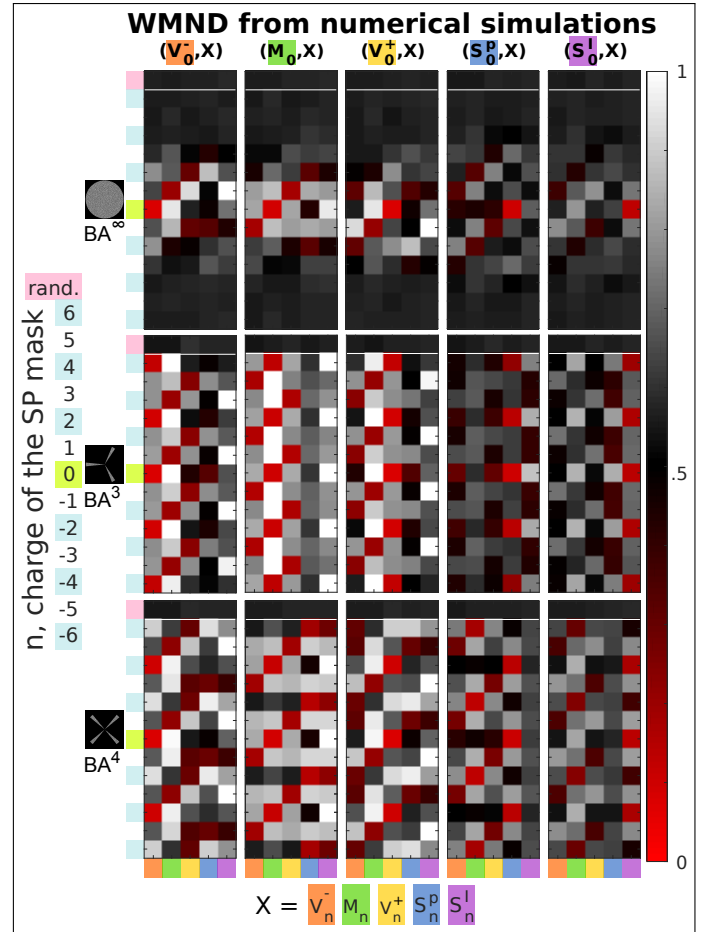

Fig. S3. Weighted Median Normalized Distance (WMND) for all possible pairs of critical points screened here, for the addition of spiral phase mask with charges up to n =±6 and for the apertures BA^N ($N \in \{3, 4, \infty\}$). The WMND were computed from numerical simulations.

C. Point group symetries of higher order

We investigated in numerical simulation the effect of an increase in the order of the dihedral point group symmetry. For this purpose, we used the apertures BA^N with $N \in \{5, 6, 7, 8\}$ (point group symmetry D_N), as defined in the main article. Because of the strong anisotropy of the central peak of its point spread function, the aperture BA^2 could not be compared to the other

apertures, and therefore was not computed. The WMND are presented in Fig. S4.

As expected for N= 5 or 6, the $\text{WMND}(Y_0, Y_{\pm N})$ are close to zero (transformation rate close to 1). We can also notice that, for BA^7 and $n \in [\![-3;3]\!]$, as well as for BA^8 and $n \in [\![-4;4]\!]$, the same $\text{WMND}(V_0^+, X_{\pm n})$ as for BA^∞ are found. The topological correlations for BA^∞ correspond to a single spiral mode, while the spiral spectrum of BA^8 contains harmonics. The first harmonics are the spiral modes $m = \pm 8$ and are for spiral modes high enough so that, for the pairs $(V_0^+, X_{\pm n})$, the topological correlations of the fundamental mode ($m = 0$ as in BA^∞) dominates for $n \in [\![-4;4]\!]$. For smaller N, the topological correlations between critical points are dictated by both the fundamental mode and the harmonics which leads to more complex WMND diagrams. This is this true in particular for BA^3 and BA^4.

D. Influence of the width of the angular slits

The influence of the width of the angular slits was investigated in numerical simulation. Simulation were performed for periodic angular slits with a point group symmetry D_3 and three different widths of angular slits were tested : $\frac{\pi}{16}$ (i.e. BA^3), $\frac{\pi}{8}$, and $\frac{\pi}{4}$. The WMND are presented in Fig. S5.

We can notice that the $\text{WMND}(Y, Y_{\pm 6})$ increases with the increasing width of the slits, and even becomes equal to 0.5 for the largest slits. This results was expected considering the spiral spectrum of the apertures. All the considered apertures have harmonics at the spiral modes $m = k.N$ with $k \in \mathbb{Z}$. However, the amplitude of the harmonics is given by a sinc apodisation function which FWHM depends on the width of the angular slits. For the angular slit $\frac{\pi}{16}$, the FWHM of the spectral apodization function corresponds to n= ± 19. As a consequence, the aperture could be considered as spectrally invariant by the addition of SP_n when n = ± 3 or ± 6. For angular slits of width : $\frac{\pi}{8}$ and $\frac{\pi}{4}$, the FWHM of the spectral apodization function corresponds to n= ± 10 and n= ± 5, respectively. Consequently, the apertures are spectrally modified by the addition of $SP_{\pm 6}$.

In the experimental procedure, the width of the angular slits was chosen large enough so that the dark center induced by the spatial sampling of the SLM pixels has a radius below 2 SLM pixels. However, the width was chosen small enough to keep a spectral invariance in the range $n \in [\![-6;6]\!]$. Both the dihedral symmetry and the width of the angular slit are important parmeters to observe the periodicity of the critical point transformation.

E. Polygonal apertures

Polygonal apertures with dihedral symmetries D_3 (equilateral triangle) and D_4 (square) were used to extend our study to other aperture shapes. The WMND computed from numerical simulations are shown in Fig. S6.

For the triangular aperture, topological correlations are observed for the pairs $(M_0, M_{\pm 3})$, but no cyclic permutation between V^-, M and $V+$ can be noticed. For the square, the WMND is very similar to the one of BA^∞ (disk). These results can be explained by the fact that, for N-gons, the Nth spiral harmonics have a much lower amplitude than the fundamental spiral mode ($m = 0$). The spiral spectrum is therefore not invariant by the addition of a SP_N mask. Moreover, for the triangular aperture, the point spread function (PSF) is an optical lattice which spatial extend expends as the charge of the SP mask increases [4]. Thereby, the maximum values of the PSF decreases, which strongly limits any possible control of the transformation of the critical points.
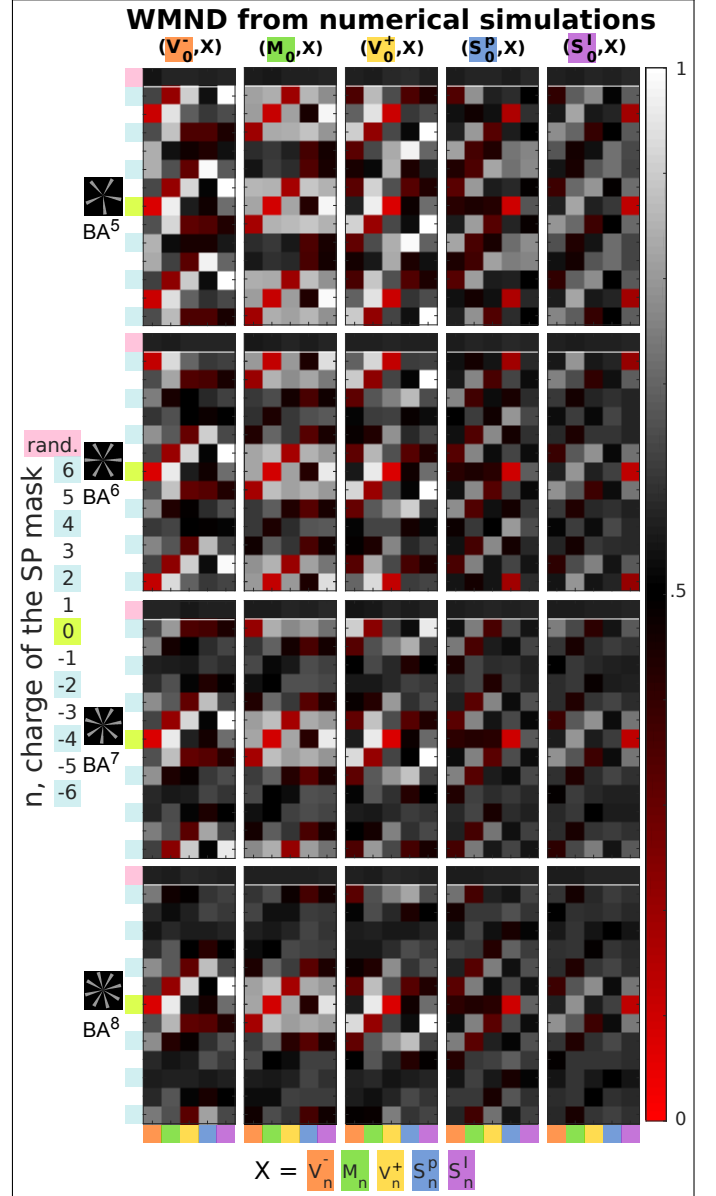

Fig. S4. WMND for all possible pairs of critical points screened here, for the addition of spiral phase mask with charges up to n =± 6 and for the apertures BA^N with N $\in \{5, 6, 7, 8\}$. The WMND were computed from numerical simulations.
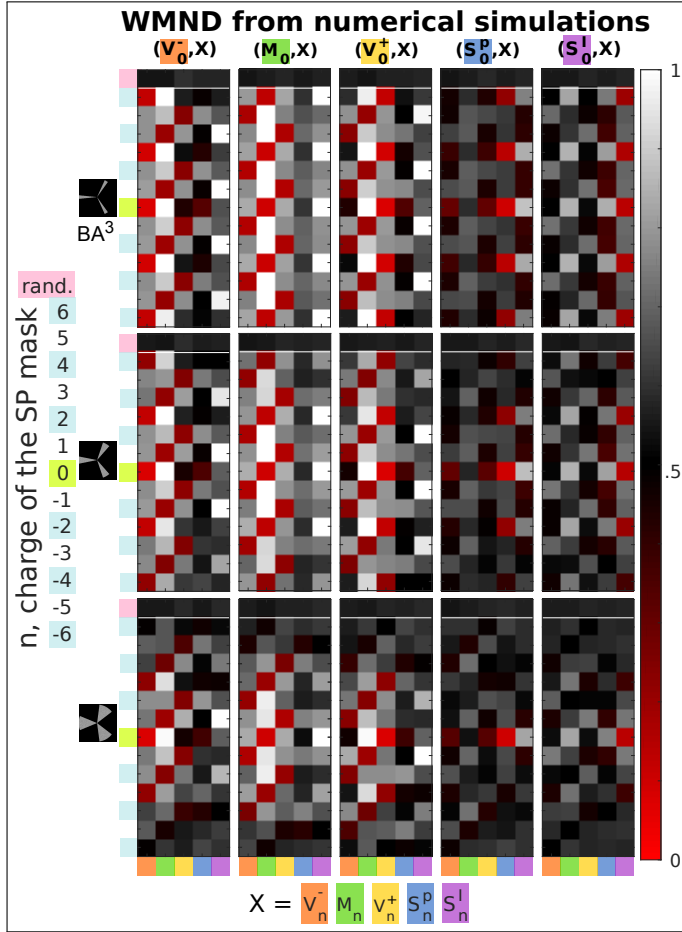
Fig. S5. Weighted Median Normalized Distance (WMND) for all possible pairs of critical points screened here, for the addition of spiral phase mask with charges up to n $=\pm6$ and for apertures with dihedral symmetry D_3 and angular slits of width : $\frac{\pi}{16}$, $\frac{\pi}{8}$, and $\frac{\pi}{4}$, respectively (from top to bottom). The WMND were computed from numerical simulations.
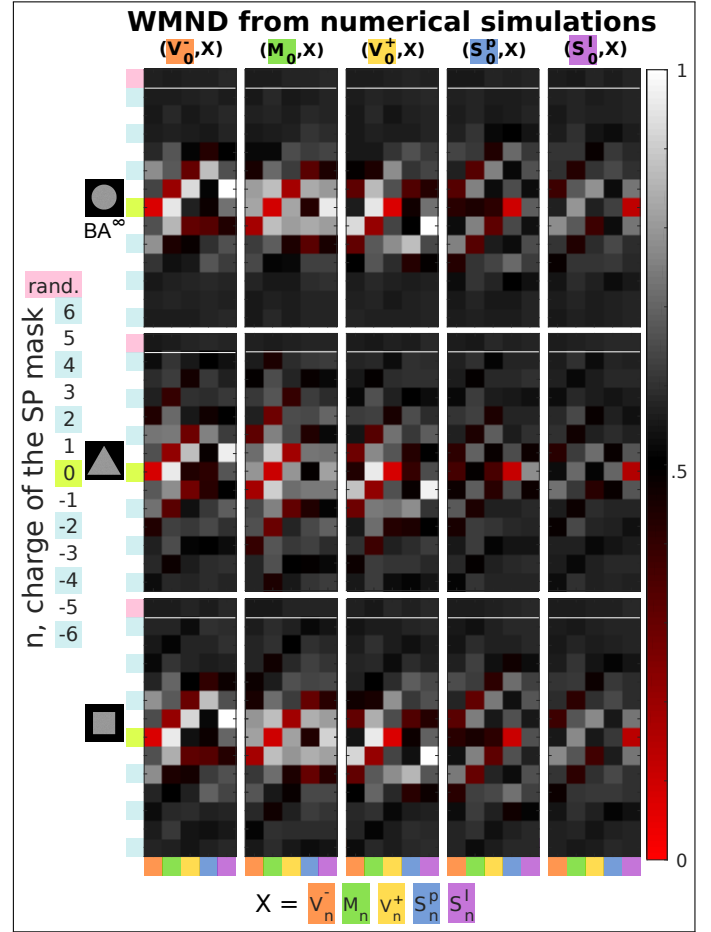
Fig. S6. WMND for all possible pairs of critical points screened here, for the addition of spiral phase mask with charges up to n $=\pm6$ and for a disk aperture (top) and polygonal apertures : equilateral triangle (dihedral symmetry D_3) and square (dihedral symmetry D_4). The WMND were computed from numerical simulations.

REFERENCES

1. D. Robinson and D. Williams, "Digital phase stepping speckle interferometry," Opt. Commun. **57**, 26 – 30 (1986).
2. K. Creath and J. Schmit, "Interferometry | phase-measurement interferometry," in *Encyclopedia of Modern Optics,* R. D. Guenther, ed. (Elsevier, Oxford, 2005), pp. 364 – 374.
3. R. Bräuer, F. Wyrowski, and O. Bryngdahl, "Diffusers in digital holography," J. Opt. Soc. Am. A **8**, 572–578 (1991).
4. J. M. Hickmann, E. J. S. Fonseca, W. C. Soares, and S. Chávez-Cerda, "Unveiling a truncated optical lattice associated with a triangular aperture using light's orbital angular momentum," Phys. Rev. Lett. **105**, 053904 (2010).